

# Lawrence Berkeley National Laboratory

## Recent Work

### **Title**

Characterization of Rare Earth Permanent Magnets

### **Permalink**

<https://escholarship.org/uc/item/0z17j3nc>

### **Authors**

Hutten, A.  
Thomas, G.

### **Publication Date**

1991-06-01



# Lawrence Berkeley Laboratory

UNIVERSITY OF CALIFORNIA

## Materials & Chemical Sciences Division

### National Center for Electron Microscopy

Presented at the 6th International Symposium on Rare Earth Magnets,  
Pittsburgh, PA, October 21-25, 1990, and to be  
published in the Proceedings

#### Characterization of Rare Earth Permanent Magnets

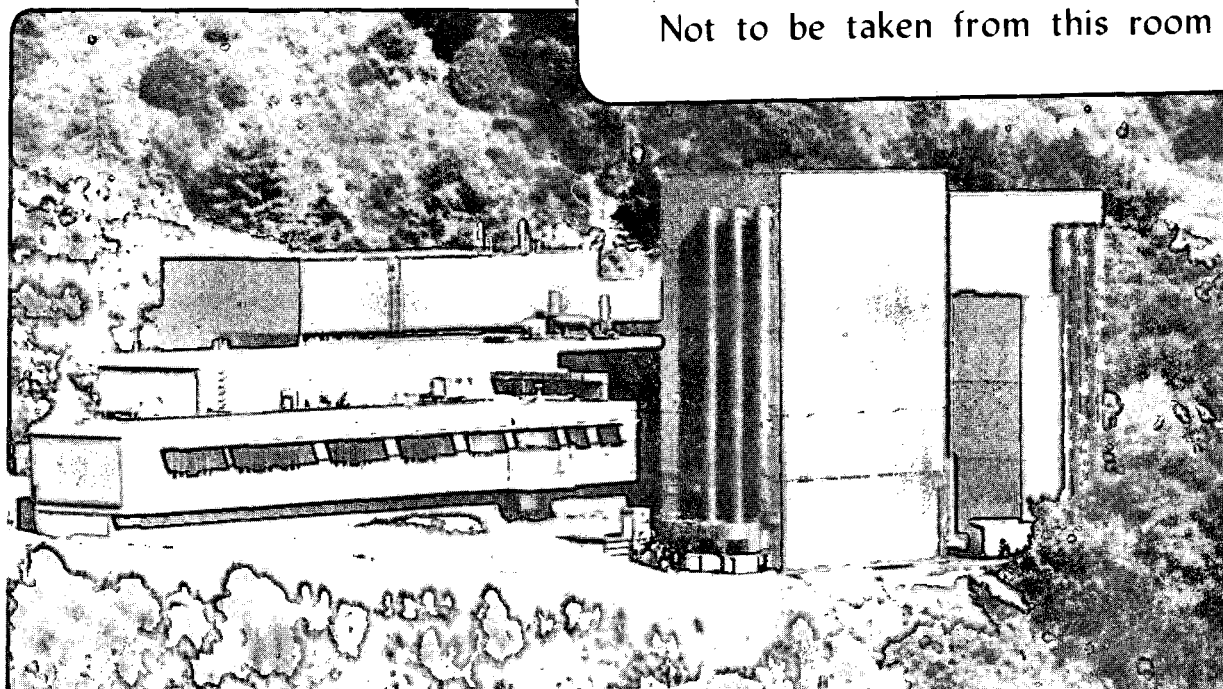
A. Hüitten and G. Thomas

June 1991

U. C. Lawrence Berkeley Laboratory  
Library, Berkeley

# FOR REFERENCE

Not to be taken from this room



Bldg. 50 Library.

Copy 1

LBL-29553

## Characterization of Rare Earth Permanent Magnets

A. Hütten and G. Thomas

Department of Materials Science  
and Mineral Engineering  
University of California

and

National Center for Electron Microscopy  
Materials Sciences Division  
Lawrence Berkeley Laboratory  
University of California  
Berkeley, California 94720

June 1991

This work was supported in part by a fellowship from the Alexander von Humboldt Foundation and by the Director, Office of Energy Research, Office of Basic Energy Sciences, Materials Sciences Division, of the U.S. Department of Energy under Contract No. DE-AC03-76SF00098.

## ABSTRACT

Recently developed alloys based either on ternary phases such as  $\text{Nd}_2\text{Fe}_{14}\text{B}$  (2-14) or on iron-rich pseudobinaries with the  $\text{ThMn}_{12}$ -structure combine excellent intrinsic magnetic properties with the appropriate microstructure for applications as hard magnetic materials. In order to understand the magnetic behavior of these materials, systematic microstructural characterization has been performed using microdiffraction, x-ray microanalyses and high resolution electron microscopy.

The magnetic behavior of three types of NdFeB specimens, namely sintered, mechanically alloyed and melt-spun, is correlated to their microstructure. The effect of minority phases on the magnetization and the coercivity in these materials is investigated. The ease with which the nonmagnetic Nd-rich grain boundary phase decouples hard magnetic "2-14" matrix grains depends on their average grain size which is related to the different preparation processes. The appearance of the nonmagnetic B-rich phase which acts as a source of local demagnetization fields is also a function of the preparation methods and can be avoided by rapid solidification.

In the SmFeMo-alloys the hard magnetic phase is tetragonal with the  $\text{ThMn}_{12}$ -structure which has about the same intrinsic magnetic properties as the "2-14". Although there are no intergranular phases in the 1-12 alloys, Sm-oxides become important as minority phases in these magnets. In comparison, SmFeTi-specimens have higher coercivities, and the origin of this is investigated as to whether any other hard magnetic phase besides 1-12 exists.

## INTRODUCTION

Rare earth permanent magnets are rapidly becoming established as important hard magnets because of their large energy products (see Table I). The Fe-Nd-B system already represents about a \$90 million dollar market in the U.S.A. However the complete potential of such magnets is still yet to be realized mainly because of the difficulties associated with their processing (control of grain size, morphology, oxidation, etc.), and because the details of the magnetic reversal mechanism(s) are not known. Materials science investigations of structure-processing-property relations are thus very necessary if the situation is to be improved. Although several efforts have already been made to study sintered and melt-spun RE alloys (<sup>1-4</sup>) the emphasis in this paper will be on mechanically alloyed FeNdB and the more recently developed SmFeTi alloys as listed in Table I.

## EXPERIMENTAL

Mechanically-alloyed specimens as well as melt-spun ribbons of nominal compositions given in Table I were provided by Siemens AG, Erlangen. The processing of these alloys of 15-40  $\mu\text{m}$  thickness and about 20-100 mm length so as to obtain ribbons in the optimum magnetic state are described in detail by Wecker and coworkers (<sup>5,6</sup>). Previous work by Schultz et al. (<sup>7,8</sup>) determined the processing parameters whereby mechanically alloyed specimens achieved optimum magnetic properties. The preparation conditions for the sintered samples are reported by Chandramouli (<sup>9</sup>).

The ribbons were mounted on a copper grid and electron transparent thin samples were made by argon ion-milling with a total gun current of 0.4 mA at liquid nitrogen temperature. Prior to ion-milling 500  $\mu\text{m}$  thick foils were cut off mechanically alloyed bulk samples. Subsequently, these foils were mechanically ground to about 100  $\mu\text{m}$  and were also mounted on copper-grids. These disks then were dimpled to a thickness of 20  $\mu\text{m}$  using a dimple grinder. A similar procedure was used for the sintered specimens. For all types of specimens the milling was completed in about 3-6 hours.

In order to characterize their microstructure by transmission electron microscopy (TEM) and microanalysis (AEM) the samples were examined using a Philips 400 electron microscope as well as a JEOL 200 CX electron microscope at the NCEM operating at 100 keV and 200 keV, respectively. Both microscopes are equipped with a Be window energy dispersive spectrometer (EDX) detector and a double tilt holder. Spectroscopic spectral deconvolution and quantification were carried out on a KEVEX 8000 system software using theoretically generated thin foil K-factors. By acquiring a minimum of  $10^5$  counts statistical significance of the data was ensured.

## RESULTS AND DISCUSSION

### Melt-Spun Ribbons:

The microstructure of specimens made by rapid solidification does not necessarily correspond to that from the expected equilibrium phases. TEM investigations of optimally quenched  $\text{Nd}_{17}\text{Fe}_{77}\text{B}_6$  ribbons by Koestler et al (<sup>10</sup>) showed a two phase microstructure consisting of the tetragonal  $\text{Nd}_2\text{Fe}_{14}\text{B}$  matrix grains with intergranular non-magnetic, crystalline  $\text{Nd}_{75}\text{Fe}_{25}$  occurring mainly at multigrain junctions. As a consequence the isolation of the hard magnetic grains by this nonmagnetic grain boundary phase is not complete. The average matrix grain size is about 80 nm diameter while 20-30% of the volume consisted of grains either less than 20 nm diameter or more than 300 nm diameter. In addition the size of the grain boundary particles is not uniform. The boron-rich  $\text{Nd}_{1.1}\text{Fe}_4\text{B}_4$  phase which is predicted by the equilibrium phase diagram was not observed. The microstructure of melt-spun  $\text{SmFe}_{10}\text{Ti}$  ribbons consists also of two phases and is shown in Figure 1. In contrast to  $\text{NdFeB}$  specimens where acceptable magnetic properties (Table I) are already achieved by direct quenching to the microcrystalline state, a subsequent heat treatment for  $\text{SmFe}_{10}\text{Ti}$  samples is necessary to obtain the magnetic values given in Table I. Figure 1A shows the typical microstructure of the as-quenched  $\text{SmFe}_{10}\text{Ti}$  specimens, while Figure 1B represents that of the annealed samples.

In contrast to the fine-grained microstructure of as-quenched specimens the average grain size of annealed specimens is about  $(30 \pm 20)$  nm. TEM and microdiffraction analyses of the annealed specimens showed that grains are

the tetragonal 1:12 phase. Using x-ray microanalysis (EDX) the average composition of these grains has been determined to be as follows: Sm ( $7.7 \pm 0.7$ ) at.%, Fe ( $84.3 \pm 0.6$ ) at.% and Ti ( $8.0 \pm 0.7$ ) at.% which is in good agreement with the expected values for the hard magnetic  $\text{SmFe}_{11}\text{Ti}$  phase. In addition, TEM analyses show the presence of a second phase which has the bcc structure with  $a_0 = (2.84 \pm 0.08)$  angstroms. EDX analyses verify that this second phase is  $\alpha\text{-Fe}$ . X-ray diffraction investigations of melt-spun  $\text{SmFe}_{10}\text{Ti}$  ribbons by Wecker et al. (6) confirm the existence of  $\alpha\text{-Fe}$ . According to Ding and Rosenberg (11), the occurrence of  $\alpha\text{-Fe}$  is due to the high vapour pressure and subsequent loss of Sm at  $T \geq 750^\circ\text{C}$ . Yamagishi et al. (12) have shown that the formation of  $\alpha\text{-Fe}$  is suppressed by annealing of the ribbon in a Sm-atmosphere.

#### Mechanically Alloyed Samples:

Mechanical alloying to produce magnets with a matrix grain size comparable with that in melt-spun magnets requires long milling times of the elemental powders, and consequently more exposure to oxidation. Hence it can be expected that the incorporation of oxygen during the processing results in a more complex microstructure. Figure 2 shows the microstructure of a mechanically alloyed and hot pressed  $\text{Nd}_{16}\text{Fe}_{76}\text{B}_8$  sample. In contrast to the two phase microstructure of melt-spun ribbons that of the mechanically alloyed  $\text{Nd}_{16}\text{Fe}_{76}\text{B}_8$  specimens is a multiphase one. The  $\text{Nd}_2\text{Fe}_{14}\text{B}$  matrix grains of about 200–800 nm in diameter contain up to 10 at.% chlorine, although its origin is unknown. In addition, two Nd-oxide phases, NdO and  $\text{Nd}_2\text{O}_3$ , and a boron-rich phase were observed by Koestler et al. (13). NdO can exist as

single crystal grains with an average grain diameter of about 200 nm and as polycrystalline regions with a diameter varying between 400 nm and 600 nm. It should be pointed out that the Nd to Fe ratio for the observed boron-rich phase is not consistent with the  $\text{Nd}_{1.1}\text{Fe}_4\text{B}_4$  phase which is predicted by the equilibrium phase diagram (14). In addition, the occurrence of two grain boundary phases,  $\text{NdFe}_2$  and a non-equilibrium Nd-rich phase have been reported by Koestler et al. (13). Mechanically alloyed and hot pressed  $\text{Sm}_{12}\text{Fe}_{78}\text{Mo}_{10}$  specimens have a similar complex microstructure (15) consisting of the tetragonal 1:12 matrix phase with an average grain size of 200–300 nm and of two Sm-oxide phases,  $\text{SmO}$  and  $\text{Sm}_2\text{O}_3$ . The microstructure is shown in Figure 3. Grains of  $\text{SmO}$  or  $\text{Sm}_2\text{O}_3$  are always larger (400–600 nm) than the 1:12 matrix grains. The most striking result is the absence of intergranular phases, even at multi-grain junctions compared to  $\text{Nd}_{16}\text{Fe}_{76}\text{B}_8$  samples. The 1:12 matrix grains contain many defects such as stacking faults and twins, which are difficult to analyze in detail due to the very small grain size.

The third mechanically alloyed, cold pressed and annealed material which has been investigated is  $\text{Sm}_{28}\text{Fe}_{62}\text{Ti}_{10}$ . Typical TEM images are shown in Figures 4a and b. An example of a TEM image of a mechanically alloyed, annealed and cold pressed  $\text{Sm}_{28}\text{Fe}_{62}\text{Ti}_{10}$  sample is displayed in Figure 4a. The average grain size is about 100–300 nm. The grains are almost all surrounded by a grain boundary phase and are thus isolated from each other. Microdiffraction analyses of this grain boundary phase revealed a fcc-structure with a measured lattice parameter of  $a_0 = (5.4 \pm 0.2)$  angstroms, which is close to that of  $\text{SmO}$ . Furthermore, EDX analyses showed that the grain boundary phase is Sm-rich. An EDX spectrum is shown in Figure 5b. No

$\text{Sm}_2\text{O}_3$ -phase is detected in these specimens so far. This indicates that  $(\text{RE})_2\text{O}_3$  is normally formed during hot pressing and therefore occurs in the other materials which are discussed above. In order to answer the question whether SmO is already formed during the milling process of the elemental powder, TEM microstructural and diffraction analyses were performed on a mechanically alloyed and cold pressed powder with the composition of  $\text{Sm}_{28}\text{Fe}_{62}\text{Ti}_{10}$ . The typical microstructure of these specimens is shown in Figure 4b. The average grain size of about  $(20 \pm 10)$  nm is small compared with that of annealed samples. The single crystal electron diffraction patterns could be indexed to be fcc with a lattice parameter of  $a_0 = (5.48 \pm 0.3)$  angstroms. This value is in agreement with the lattice parameters of SmO as found in annealed specimens. Therefore, it can be concluded that SmO is formed already during the milling process.

Figure 5 shows that besides the SmO grain boundary phase, other phases of the annealed specimens are detected by EDX using a regular Be window detector. The average compositions of these phases are summarized in Table II. Microdiffraction analyses of the Ti-enriched phase revealed a hexagonal structure with lattice parameters  $a = (4.7 \pm 0.2)$  angstroms and  $c = (7.9 \pm 0.2)$  angstroms which correspond to the structure of  $\text{TiFe}_2$ . Figure 5 shows EDX spectra from these phases, from which the composition of the Sm-enriched phase with about 23 at.% Sm can be described as  $(\text{Sm},\text{Ti})\text{Fe}_3$ . Microdiffraction analyses were inconclusive in determining the structure of this phase. Figure 5 shows that  $\text{TiFe}_2$  and  $(\text{Sm},\text{Ti})\text{Fe}_3$  grains occur frequently, unlike the second Sm-enriched phase. It should be pointed out that in these EDX experiments the detector was incapable of detecting oxygen. Therefore, it is not yet proved whether the Sm-rich phases are oxygen stabilized or not.

However, the ubiquitous presence of oxygen surface layers which are expected at rare-earth enriched grains makes it very difficult to determine accurately the bulk oxygen content. The major result is that neither the hard magnetic 1:12 phase nor the new hard magnetic  $\text{Sm}_7(\text{Fe,Ti})_3$  phase with hexagonal structure ( $a = 8.76$  angstroms,  $c = 25.62$  angstroms) which is observed by Kemprath et al (16) are found so far in this material.

### Sintered Specimens:

Microdiffraction and EDX-analyses confirmed that the microstructure of sintered  $\text{Nd}_{11}\text{Fe}_{75.3}\text{B}_{5.1}\text{Dy}_{6.4}\text{Al}_{1.5}$  specimens consist of  $\text{Nd}_2\text{Fe}_{14}\text{B}$  grains 5–10  $\mu\text{m}$  in diameter with primarily single crystal fcc NdO at grain boundary junctions. Figure 2a shows a typical multigrain junction. According to Chandramouli (9) Dy is incorporated into the  $\text{Nd}_2\text{Fe}_{14}\text{B}$  matrix phase, and is enriched in large inclusions which are formed in the region near the grain boundary.

The comparison between the average size of hard magnetic grains of different materials and the single-domain size of the corresponding hard magnetic phase (Table I) indicates that mechanical alloying as well as melt-spinning are the favored techniques to produce a microstructure with grain sizes corresponding to that of single domains. These calculated single domain sizes can be interpreted only as a lower estimation (17), and so it is likely that the critical size  $D_c$  (Table I) is larger than the observed average grain size in the investigated materials which were prepared by one of these methods. The observed coercivity, on the other hand, is less than that predicted for a single-domain particle behavior. Hence the question arises

which are the limiting microstructural factors which prevent the approach to optimum magnetic properties.

In the case of the melt-spun  $\text{Nd}_{17}\text{Fe}_{77}\text{B}_6$  ribbons the nonmagnetic  $\text{Nd}_{75}\text{Fe}_{25}$  grain boundary phase occurs mainly at multigrain junctions. The efficiency of magnetic coupling between neighboring hard magnetic grains is therefore less than that expected for a microstructure in which the hard magnetic grains are completely isolated by a nonmagnetic grain boundary phase. Although the observed 1:12 phase in melt-spun  $\text{SmFe}_{10}\text{Ti}$  samples have comparable magnetic properties to those of the 2:14 phase in  $\text{Nd}_{17}\text{Fe}_{77}\text{B}_6$  specimens, the coercivity of the former material is very low. According to the results the low coercivity must be due to the presence of the soft magnetic  $\alpha\text{-Fe}$  in this material. The incorporation of up to 10 at.% Cl into the  $\text{Nd}_2\text{Fe}_{14}\text{B}$  phase of mechanically alloyed  $\text{Nd}_{16}\text{Fe}_{76}\text{B}_8$  samples may reduce its magnetocrystalline anisotropy and hence the coercivity. In addition, the existence of large polyhedral rare-earth oxide grains may act as sources of local demagnetization fields and hence contribute to a reduction of the coercivity.

The low coercivity value of mechanically alloyed  $\text{Sm}_{12}\text{Fe}_{78}\text{Mo}_{10}$  specimens can be explained by the absence of any grain boundary phase. The magnetic 1:12 grains are therefore not separated from each other which leads to magnetic coupling between neighboring grains. Moreover, the absence of an isolating grain boundary phase lowers the barrier height for domain wall propagation. The influence of the observed rare-earth oxides as sources of demagnetizing stray fields in such a microstructure is even greater. Whether the high intragranular defect concentration in the hard magnetic grains can

compensate for the absence of any grain boundary phase by domain wall pinning has yet to be studied in detail. The coercivity of mechanically alloyed  $\text{Sm}_{28}\text{Fe}_{62}\text{Ti}_{10}$  samples reaches values of up to 60 kOe although the observed Ti-substituted  $\text{Fe}_2\text{Sm}$  and  $\text{Fe}_3\text{Sm}$  phases cannot be the origin for such high coercivity. On the other hand, these grains are completely surrounded by a nonmagnetic SmO-phase. This microstructure therefore represents close to an ideal one with noninteracting single domain particle grains. This conclusion is now being further examined using Lorentz imaging to study the magnetic domain configuration.

The average grain size in the investigated sintered samples is of the order of 2 magnitudes greater than the calculated critical domain size. Therefore, the existence of grains with multi-domains already in the state of remanence can be expected. The incorporation of Dysprosium in the hard magnetic grains can result in an increase in the nucleation field of this phase. The presence of large rare-earth inclusions around the grain boundaries on the other hand may compensate for this effect by influence on demagnetizing stray field sources.

Although these electron microscopy and analytical techniques successfully provide microstructural information, the interaction of domain walls with the microstructure, especially in those fine-grained materials, is not fully understood. Unfortunately, instrumentation is not yet available for high resolution characterization to be made of the magnetic structure (eg. domain walls) and its interaction with the microstructure, although low resolution qualitative Lorentz imaging can sometimes be useful. Some of the background relating to these problems are discussed in recent papers (18,19). Some

examples of magnetic materials are discussed in Ref. 20.

### ACKNOWLEDGEMENTS

The authors gratefully acknowledge Drs. L. Schultz and J. Wecker for providing the samples used in this study. The technical assistance of M. Chandramouli and C.J. Echer on electron microscopy is appreciated.

This work is partially supported by the Director, Office of Basic Energy Sciences, Materials Science Division of the U.S. Department of Energy under contract number DE-AC03-76SF00098. A. Hütten acknowledges a fellowship from the Alexander von Humboldt-Foundation, West Germany.

## REFERENCES

1. K.H. J. Buschow, Material Science Report 1 (1986).
2. H. Kronmüller, K.D. Durst and M. Sagawa, J. Magn. Magn. Mat. 74 (1988) p. 291.
3. J.D. Livingston, J. Appl. Phys. 57 (1985) p. 4137.
4. R. Ramesh, J.K. Chen, L.K. Rabenberg and G. Thomas, Proc. ASM Symposium on Hard and Soft Magnetic Materials, Cincinnati, Ohio, U.S.A., 1987, p. 1.
5. J. Wecker and L. Schultz, J. Appl. Phys. 62 (1987), p. 990.
6. J. Wecker, M. Katter, K. Schnitzke and L. Schultz, J. Appl. Phys. 67 (1990), p. 4951.
7. L. Schultz, J. Wecker and E. Hellstern, J. Appl. Phys. 61 (1987) p. 3583.
8. L. Schultz, K. Schnitzke and J. Wecker, J. Magn. Magn. Mater. 83 (1990) p. 254.
9. M. Chandramouli, Proc. XIIth Intl. Conf. for Electron Microscopy, Seattle, WA, U.S.A., 1990, p. 990.
10. C. Koestler, R. Ramesh, C.J. Echer, G. Thomas and J. Wecker, Acta Met. 37 (1989) p. 1945.
11. J. Ding and M. Rosenberg, J. Magn. Magn. Mat. 83 (1990), p. 257.
12. K. Yamagishi, M. Okada and M. Homma, Proc. 10th Intl. Workshop on Rare-Earth Magnets and Their Applications, Kyoto, Japan, 1989, p. 217.
13. C. Koestler, M. Chandramouli and G. Thomas, to be published in J. Magn. Magn. Mat.
14. G. Schneider, E.T. Henig, G. Petzow and H.H. Stadelmaier, Z. Metallkde, (1986), p. 755.

15. C. Koestler, L. Schultz and G. Thomas, J. Appl. Phys. 67 (1990), p. 2532.
16. N. Kamprath, X.R. Qian, H. Hedge and F.J. Cadien, J. Appl. Phys. 67 (1990), p. 4948.
17. H. Sun, Y. Otani, J.M.D. Coey, C.D. Meekison and J.P. Jakubovics, J. Appl. Phys. 67 (1990), p. 4659.
18. R. Ramesh, G. Thomas and B.M. Ma, Proc. of the MRS Intl. Meeting on Advanced Materials, Vol. 11 (1988) p. 35.
19. Proc. DOE Workshop on Magnetic Materials, Material Sciences Engineering, B3 (1989).
20. R. Ramesh and G. Thomas, Material Sciences and Engineering, B3 (1989) p. 435.

## FIGURE CAPTIONS

Figure 1 : TEM micrographs of melt-spun  $\text{SmFe}_{10}\text{Ti}$  ribbons.

A : fine-grained microstructure of as quenched samples.

B : microstructure after annealing at  $810^\circ\text{C}$  for 15 min.

Figure 2: Comparison of microstructures :

a. TEM micrograph of multigrain junction

(  $\text{M}=\text{Nd}_2\text{Fe}_{14}\text{B}$ ,  $\text{RE}=\text{Dy}$ -rich inclusion ).

b. TEM image of mechanically alloyed  $\text{Nd}_{16}\text{Fe}_{76}\text{B}_8$  showing the 2-14-1 matrix grains, single crystal NdO grains are labeled “a”; and polycrystalline NdO regions are labeled “b”.

c. TEM image of melt-spun  $\text{Nd}_{17}\text{Fe}_{77}\text{B}_6$  quenched into the optimum magnetic state.

Figure 3 : TEM micrograph showing a small single-crystal fcc SmO grain are labeled

“SC” and four polycrystalline fcc SmO grains (marked by arrows).

The fcc structure of the polycrystalline variant is illustrated by the inserted microdiffraction pattern. N indicates tiny nuclei of the SmO phase.

Figure 4 : TEM images of mechanically alloyed  $\text{Sm}_{28}\text{Fe}_{62}\text{Ti}_{10}$  powder.

B : as mechanically alloyed and cold pressed.

A : annealed for 30 min at  $850^\circ\text{C}$ .

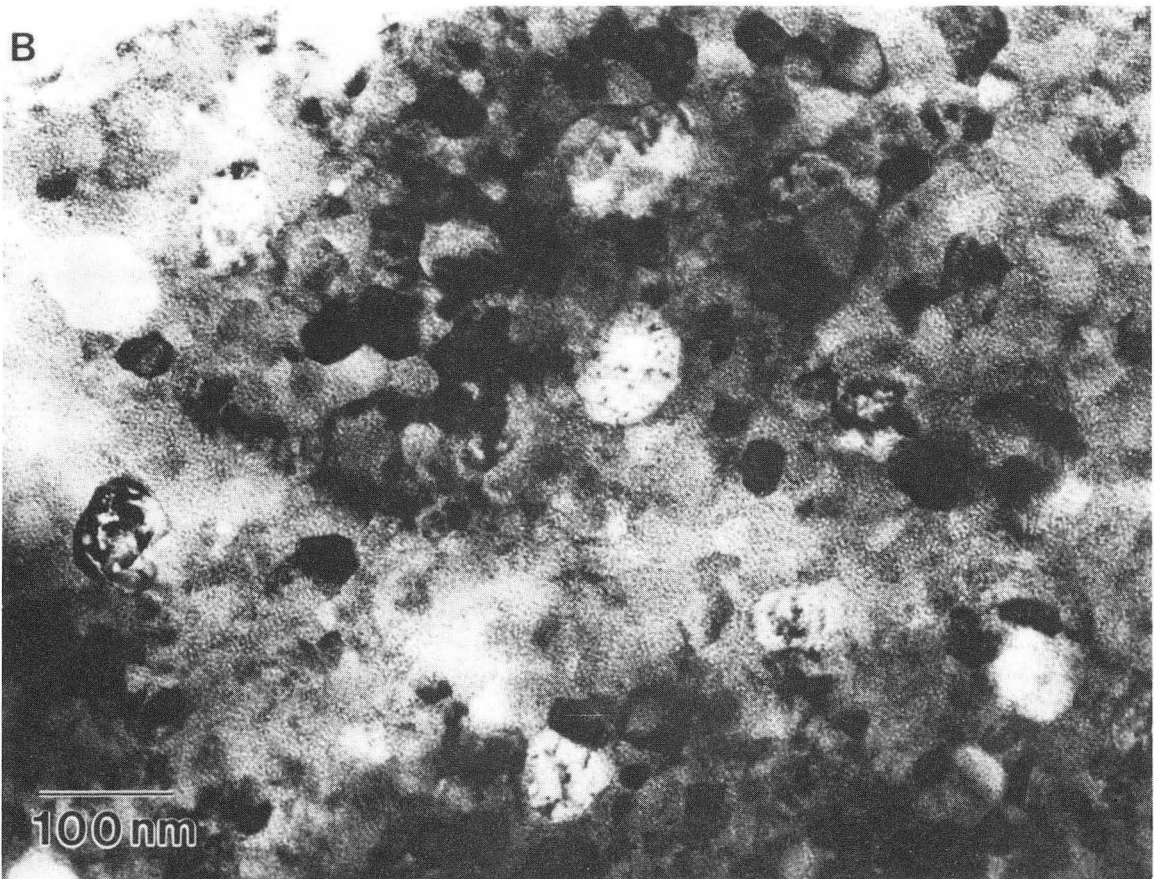
Figure 5 : TEM micrograph and EDX spectra of mechanically alloyed and at  $850^\circ\text{C}$

for 30 min annealed  $\text{Sm}_{28}\text{Fe}_{62}\text{Ti}_{10}$ . Sm substituted  $\text{Fe}_2\text{Ti}$  grains “A”

and Ti substituted  $\text{Fe}_3\text{Sm}$  grains “B” are surrounded by a SmO

grain boundary phase. EDX spectra of (A) the “ $\text{Fe}_2\text{Ti}$ ” and (B) the

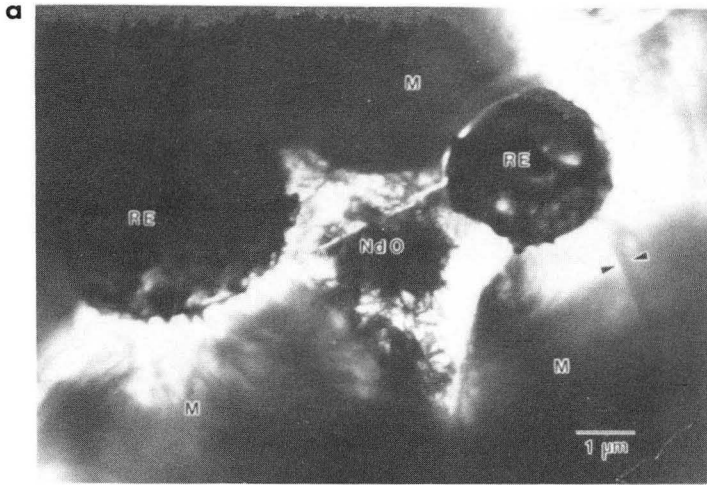
$\text{Fe}_3\text{Sm}$  and (GB) the SmO phase.



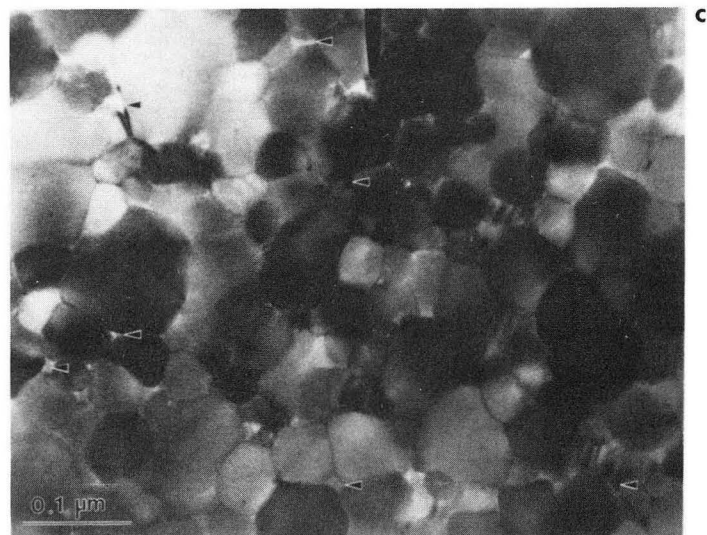
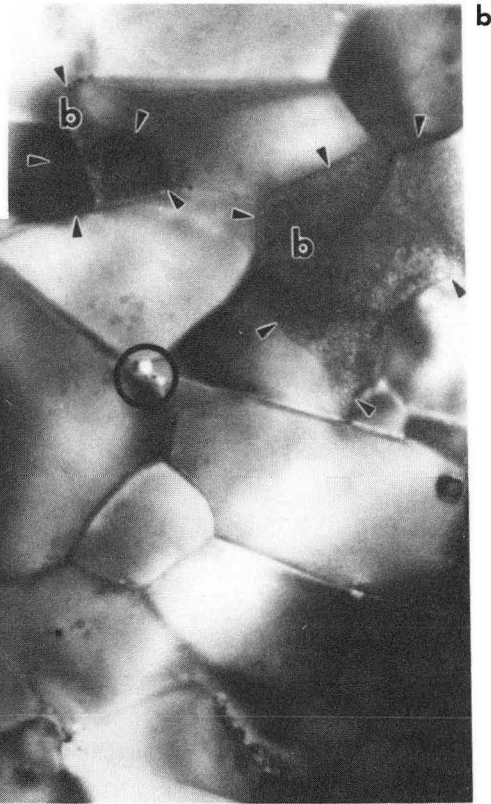
XBB 908-6886

Fig. 1

Sintered  
 $\text{Nd}_{11}\text{Dy}_{6.4}\text{Fe}_{75.3}\text{B}_{5.8}\text{Al}_{1.6}$

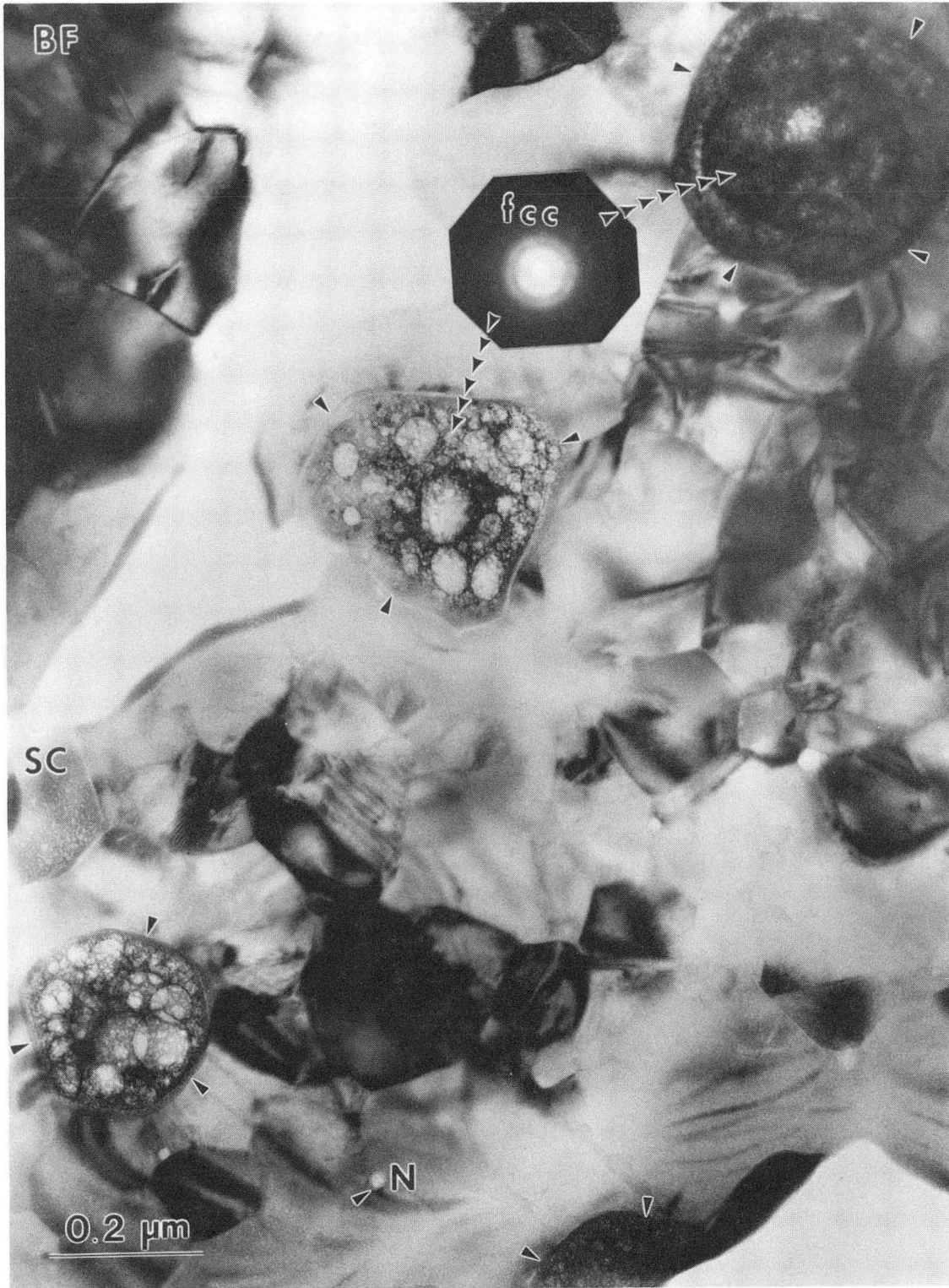


Mechanically alloyed  
 $\text{Nd}_{16}\text{Fe}_{76}\text{B}_8$



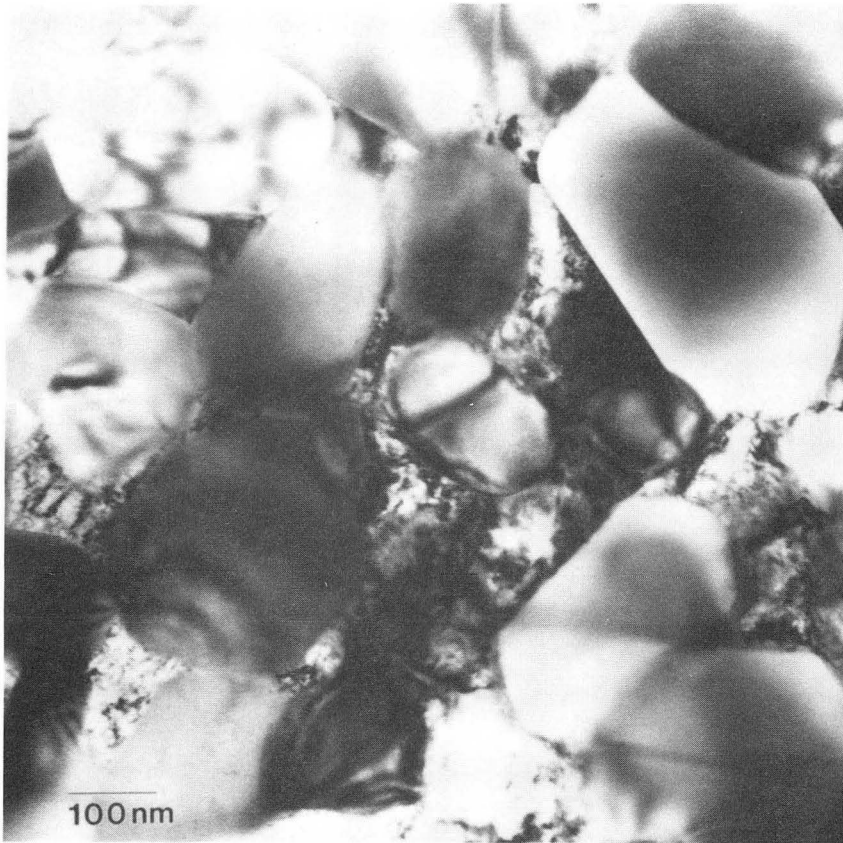
Melt-spun  
 $\text{Nd}_{17}\text{Fe}_{77}\text{B}_6$

XBB 880-9823A

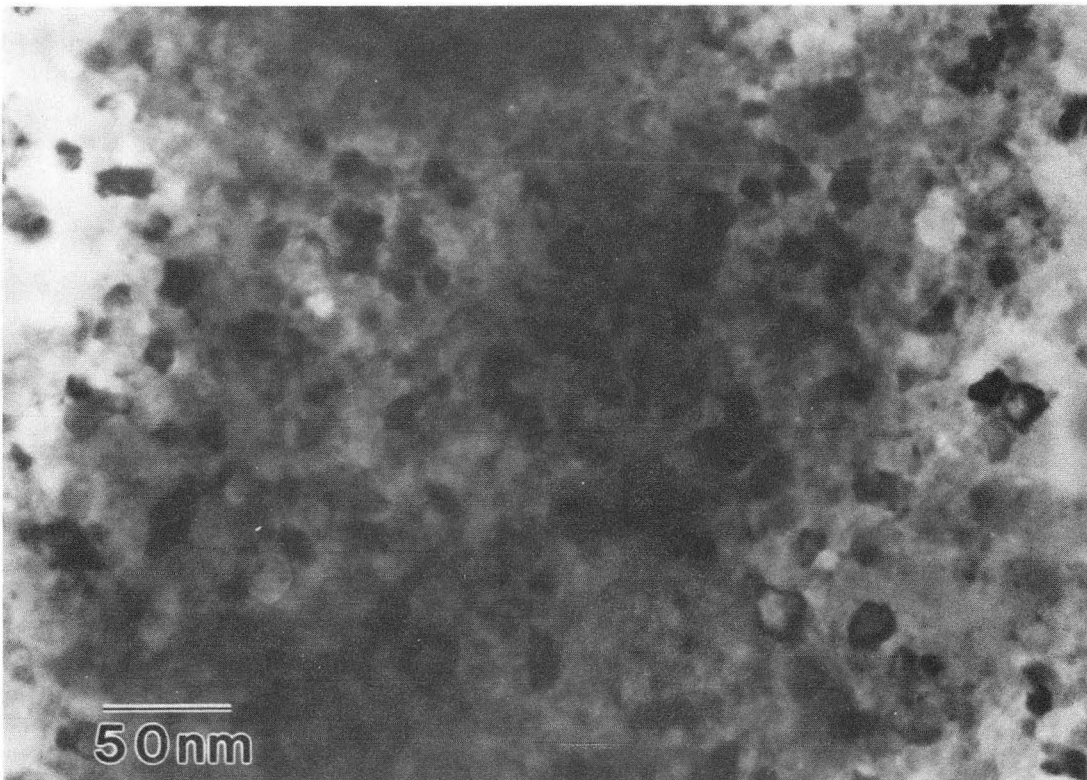


XBB 892-1325

A

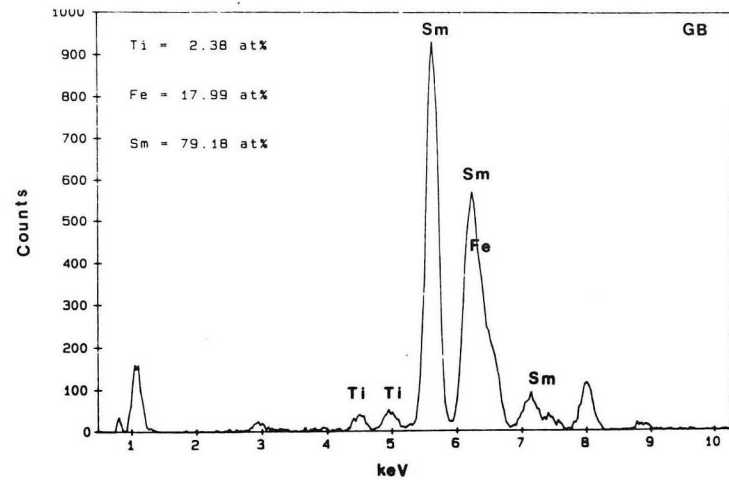
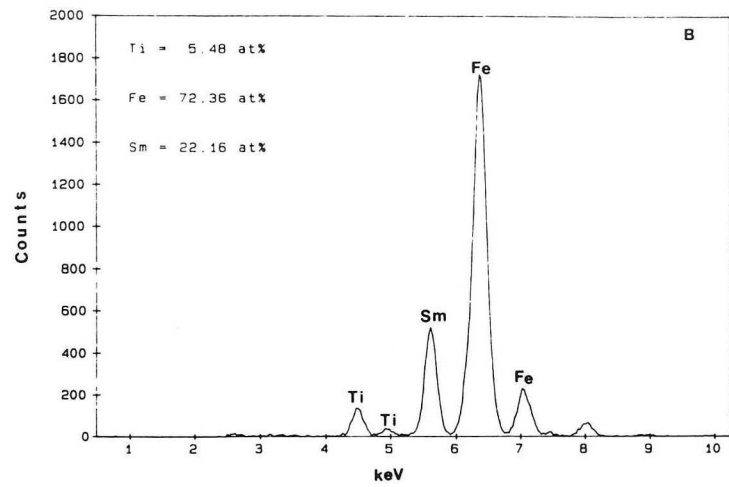
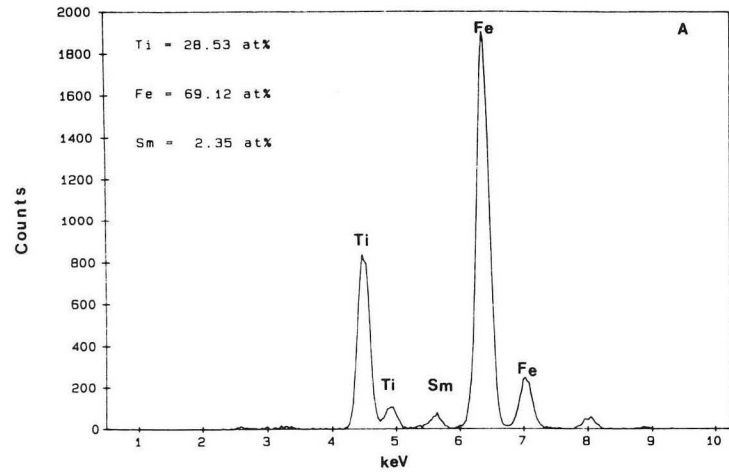


B



XBB 908-6888A

$\text{Sm}_{28}\text{Fe}_{62}\text{Ti}_{10}$  - 850°C / 30 min



XBB 908-6887B

Fig. 5

TABLE I: Microstructural and magnetic properties of the investigated samples

	$H_{ic}$ (kOe)	$B_r$ (kG)	BH(MGOe)	$D_c^*$ (nm)	$D^{**}$ (nm)	GB-phase <sup>+</sup>
<b><u>Sintered:</u></b>						
<b>Nd<sub>11</sub>Dy<sub>6.4</sub>Fe<sub>75.3</sub>B<sub>5.8</sub>Al<sub>1.6</sub>:</b>						
	25	10.3	46	200	5-10 $\mu$ m	none
<b><u>Mechanically alloyed:</u></b>						
<b>Nd<sub>16</sub>Fe<sub>76</sub>B<sub>8</sub>:</b>						
and hot pressed	15.8	6.8	10.1	80-120	200-800	present
<b>Sm<sub>12</sub>Fe<sub>78</sub>Mo<sub>10</sub>:</b>						
and hot pressed	3.8	4.0	3.8	140-160	200-300	none
<b>Sm<sub>28</sub>Fe<sub>62</sub>Ti<sub>10</sub>:</b>						
annealed and cold pressed	60.7	2.6	1.6		170 $\pm$ 95	present
<b><u>Melt - spun:</u></b>						
<b>Nd<sub>17</sub>Fe<sub>77</sub>B<sub>6</sub>:</b>						
optimally quenched	20.0	6.4		80-160	80	present
<b>SmFe<sub>10</sub>Ti:</b>						
as quenched and annealed	3.3	5.9	3.7	54	30 $\pm$ 20	none

\* single domain size \*\* average matrix grain size + presence of grain boundary phase

LAWRENCE BERKELEY LABORATORY  
UNIVERSITY OF CALIFORNIA  
INFORMATION RESOURCES DEPARTMENT  
BERKELEY, CALIFORNIA 94720